



Numerical Simulation of Crossflow-Transition Control using Pinpoint Suction

Tillmann A. Friederich and Markus J. Kloker

Abstract Laminar-turbulent transition in swept-wing boundary layers is typically caused by secondary instabilities of steady crossflow vortices (CFVs). So far, suction for laminar flow control (LFC) in three-dimensional boundary layers has been applied to reduce the crossflow and thus the growth of the primary CFV modes to CFVs. We investigate the influence of strong, localized suction (*pinpoint suction*) on developed high-amplitude CFVs and their secondary instability. By means of direct numerical simulation we show the successful application of pinpoint suction resulting in a significant delay of transition. Strong suction at the wall turned out to require an extremely small wall-normal grid spacing near the wall for our incompressible vorticity-based code *N3D*. For verification of the results a comparison with our compressible code *NS3D* has been performed.

1 Introduction

During the last decades both ecological and economical reasons lead to a strong demand on LFC technology development. Little potential is thought to be left in research areas like enhanced shaping and higher surface quality of wetted areas or engine improvement, but the overall drag of a current airliner with nearly fully turbulent flow could be reduced by 16% if the flow over 40% of the surfaces were laminar [12]. Nowadays, the two-dimensional breakdown caused by Tollmien-Schlichting (T-S) waves can be successfully controlled, see e.g. [10] (albeit not yet applied at airliners cruise conditions). In a three-dimensional boundary layer however the physical mechanism of transition to turbulence is completely different and methods like T-S wave cancelation cannot be applied.

Detailed studies on the three-dimensional transition process have been carried out in the last decades: Experiments [16], theoretical results [7] and DNS [14, 15] entirely revealed the secondary instability mechanism of CFVs. Several control methods have been developed since: Saric et al. [11] proposed the distributed roughness elements method (DRE), where a one-time excitation of closely spaced steady CFVs generates a (secondarily) more stable flow scenario and thus delays transition. The

Tillmann A. Friederich
e-mail: friederich@iag.uni-stuttgart.de

Markus J. Kloker
e-mail: kloker@iag.uni-stuttgart.de

Institut für Aerodynamik und Gasdynamik, Universität Stuttgart, Pfaffenwaldring 21, D-70550 Stuttgart, Germany

concept of upstream flow deformation (UFD), suggested by Wassermann & Kloker [13, 14], pursues the same goal, not necessarily connected to roughness.

Messing & Kloker [9], [6] proposed a combination of UFD and suction, called distributed flow deformation (DFD) or formative suction, that aims at a persistent suppression of (secondarily) unstable CFVs in altering base flows.

Investigations by Bonfigli & Kloker [3] revealed that the amplification of secondary instability modes of CFVs depends rather strongly on the wall-normal velocity component of the underlying base flow which lead to the initial idea of pinpoint suction by Friederich & Kloker [4].

Up to now all results including pinpoint suction have been obtained using our well-tested incompressible code *N3D*. As it turned out the code needs an extremely well-resolved wall-normal grid at the wall when *strong* suction is applied. This is due to the vorticity formulation and the strong velocity gradients at the wall connected to a large wall-normal velocity component at the wall. In this paper we compare results for one selected pinpoint-suction case with results from our compressible code *NS3D* to verify our converged incompressible results.

2 Numerical Methods and Simulation Setups

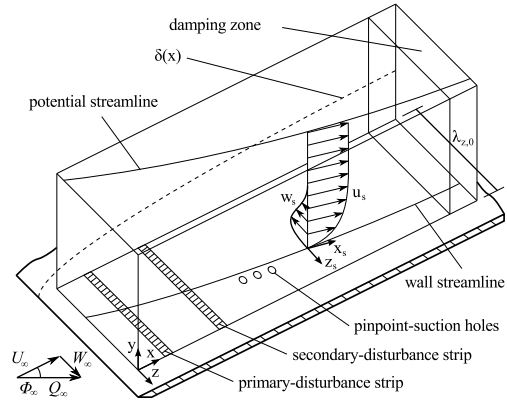
For both numerical methods all flow variables are non-dimensionalised with reference values including the reference length \bar{L} , velocity \bar{U}_∞ , Reynolds number $Re = \bar{U}_\infty \bar{L} / \bar{\nu}_\infty$ and in addition for the compressible case \bar{T}_∞ and $\bar{\rho}_\infty$ where the bar denotes dimensional values.

2.1 Incompressible Code *N3D*

N3D solves the incompressible three-dimensional Navier-Stokes equations in velocity-vorticity formulation. All flow quantities are split into a steady part (base flow) and an unsteady part $q = q_B + q'$ to ease the formulation of boundary conditions. Note that the time mean $\langle q' \rangle$ is non-zero for large q' . Sixth-order compact finite differences are used to discretize the streamwise (x) and wall-normal (y) directions. A Fourier spectral ansatz with $KMAX + 1$ modes is chosen for the spanwise direction z , where the fundamental wavelength is defined as $\lambda_z = 2\pi/\gamma_0$. The integration domain is shown in Fig. 1, and for the detailed method see [14] and [3].

Instead of using our explicit standard fourth-order Runge-Kutta time-integration scheme a semi-implicit method has been developed due to the prohibitive viscous time-step limit caused by the necessary fine y -resolution at the wall. A three-stage second-order predictor-corrector method has been set up that is based on Heun's method with an additional corrector step to secure A-stability for the explicitly treated convective terms. In this method the viscous terms in wall-normal direction are simultaneously treated by the fully implicit trapezoidal rule. In addition, an iteration method is necessary for the vorticity equations at the wall (see Eq. 2.15 in [14]). The convective terms in y -direction still impose a small time step that required the implementation of a spatial filter in x -direction since the slightly dissi-

Fig. 1 Integration domain, body-fixed (x, y, z) and streamline-oriented (x_s, y, z_s) coordinate systems.



pative forward-backward differencing for the convective terms in x -direction did not provide enough damping of high wavenumber modes due to the small time step.

2.2 Compressible Code NS3D

NS3D solves the compressible three-dimensional Navier-Stokes equations in conservative formulation and total variables where $\mathbf{Q} = (\rho, \rho u, \rho v, \rho w, E)^T$ represents the solution vector. The specific heat capacities c_p and c_v as well as the Prandtl number are assumed to be constant whereas temperature-viscosity dependence is modeled by Sutherland's law. Similarly to the incompressible code a rectangular integration domain on a flat plate is considered with similar nomenclature and discretization. In contrast to *N3D*, *NS3D* computes mainly in physical space and the Fourier space is used for obtaining the z -derivatives only. For time integration a standard explicit fourth-order Runge-Kutta method is used. For numerical details see [1] and [8].

2.3 Implementation of Suction

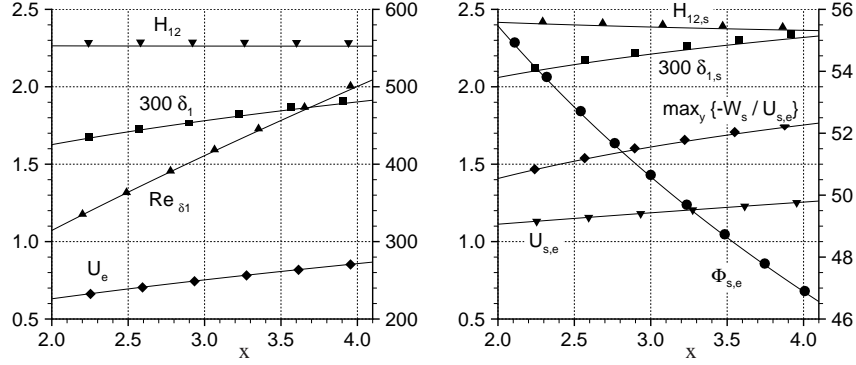
For both codes the suction holes are modeled using fixed wall boundary conditions: The wall-normal velocity component $v|_{wall}$ (*N3D*) or the wall-normal momentum $\rho v|_{wall}$ (*NS3D*) are prescribed with a $\cos^3(r)$ -function where r is the radial coordinate such that the maximum velocity in the hole center is $v/U_\infty = 0.5$. For the compressible case, this is checked in a post-processing step (and in case corrected by updating ρv). Details on the suction implementation can be found in [9].

2.4 Base Flows and Simulation Setups

A reference case and a pinpoint-suction case are evaluated for both the incompressible and the compressible code, namely cases *REF_i*, *REF_c*, *PP_i*, and *PP_c*. The base flow is taken from the DLR-Prinzipexperiment Göttingen [2], see also Bonfigli & Kloker [3]. The free-stream velocity \bar{U}_∞ was 14 m/s in the experiment, with cord-wise Mach number $Ma_\infty \approx 0.04$. For *NS3D* $Ma_\infty = 0.21$ has been chosen since the time-step limit is approximately proportional to Ma for low Ma , and still to ensure

Table 1 Simulation parameters.

	<i>incompressible setup</i>	<i>compressible setup</i>
x_0	1.655	1.900
$\Delta x \times 10^3$	1.309	1.309
$\Delta y_{wall} \times 10^4$	0.066	2.300
$\Delta y_e / \Delta y_{wall}$	120	12
y_e	0.077	0.116
$\Delta z \times 10^3$	3.747	3.747
KMAX	10	10
γ_0	52.400	52.400
$\Delta t \times 10^5$	6.550	1.047
grid points $x \times y \times z$	$2162 \times 225 \times 32$	$1816 \times 95 \times 32$
Re	92000	92000
\bar{L}	0.10 m	0.0197 m
\bar{v}_∞	$1.5 \cdot 10^{-5} \text{ m}^2/\text{s}$	$1.5 \cdot 10^{-5} \text{ m}^2/\text{s}$
\bar{U}_∞	14.00 m/s	71.03 m/s
$\bar{W}_\infty = W_e$	12.83 m/s	65.09 m/s
Ma_∞	-	0.21
$\bar{T}_\infty = T_{wall}$	-	288.15 K
\bar{p}_∞	-	0.9649 bar
Φ_∞	42.5°	42.5°

**Fig. 2** Boundary layer parameters for the incompressible (lines) and compressible base flow (symbols). Right ordinates show Re_{δ_1} and $\Phi_{s,e}$, respectively. Values in the right plot are based on $U_{s,e}$.

predominantly incompressible behaviour. The integration domains cover the same Re_{δ_1} range to ensure flow similarity. Simulation parameters are summarized in Table 1 and a comparison of the respective boundary-layer parameters is provided in Fig. 2.

The compressible base flow is computed with *NS3D* using a solution of the parabolized Navier-Stokes equations as initial condition where the free-stream velocity $U_e(x)$ is chosen as design variable and prescribed to be identical to the incompressible case.

Note that the base flows are two-dimensional (infinite wing-span assumption), but include a spanwise velocity component W , where the edge velocity W_e is kept constant. For the compressible case the temperature T_b and density ρ_b vary less than by 0.5% within our integration domain.

3 Secondary Instability and Pinpoint Suction Concept

At $x = 2.2$ the unstable primary crossflow vortex mode $(0,1)$ is triggered (we use the common double-spectral notation (h,k) , where frequencies $\beta = h \cdot \beta_0$ and spanwise wave numbers $\gamma = k \cdot \gamma_0$). After the crossflow vortex has developed to a finite amplitude level, a pulse-like disturbance containing frequencies between $\beta = 6.0$ and $\beta = 300.0$ with $\Delta\beta = 6.0$ is periodically excited at $x = 3.0$ to initiate controlled secondary instability (case REF_i). Fig. 3 shows the pinpoint suction setup. The main crossflow vortex (marked by the dashed λ_2 values, right) is turning clockwise (looking downstream). The eigenfunction of the typical unstable secondary instability mode with $\beta = 90$ is concentrated at the location of the high-shear layer at the up-draft side of the vortex. Clearly, the suction hole position (marked by the arrows) is right beneath this layer.

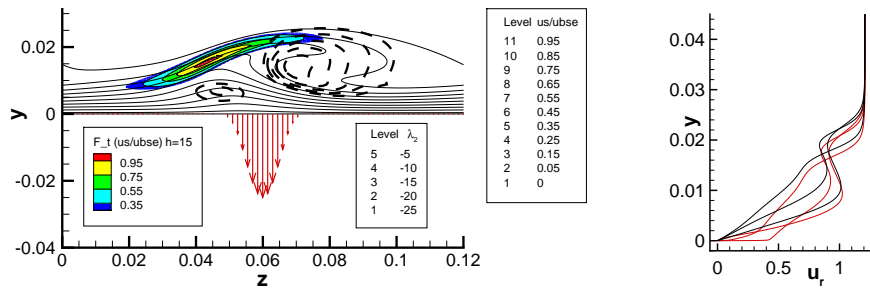


Fig. 3 Left: Pinpoint suction concept: Crosscut at $x = 3.36$ through a crossflow vortex without suction (lines: \tilde{u}_s -isocontours; dashed lines: λ_2 -isocontours; colored: modal \tilde{u}_s -amplitude distribution of high-frequency secondary instability mode $h=15$) and design example of pinpoint-suction position at the wall (arrows, crosscut through center of suction hole). Right: u_r -velocity profiles above the suction hole (black: reference case, red: suction case). The profiles are located at $x_r = 1.32$ and $z_r = 0.03, 0.04, 0.05$ (cf. Fig. 5).

4 Results

For a maximum suction velocity of $v/U_\infty = 0.5$ within the holes the incompressible simulation demands an extreme wall-normal resolution of $\Delta y_{wall} \approx \frac{1}{1100} \delta_1$ for converged results to adequately capture the occurring large gradients (see Fig. 3, right). Since there are - to the authors' knowledge - no publications on strong suction in three-dimensional boundary layers available our compressible numerical method is chosen as verification source since it solves a different set of equations with different numerics and coding.

The compressible simulation is carried out triggering identical perturbations as in the incompressible case (primary mode, secondary modes, see Sec. 3) resulting in case REF_c . The downstream amplitude development of selected steady and unsteady modes of the streamline-oriented disturbance velocity component $\tilde{u}_s = u_s/U_{b,s,e}$ is shown in Fig. 4 (comparing black lines for case REF_i and black symbols for case REF_c). Almost no differences for the steady modes can be observed: The development of the purely three-dimensional steady deformation $\beta = 0 - (0,0)$, serving

as measure for the vortex strength, is nearly identical as well as the steady two-dimensional deformation $(0,0)$ and as an example for a spectral mode $(0,3)$ reveals no deviations as well. The unsteady modes seem to have a slightly different receptivity which is most likely due to weakly deviating v -velocity profiles of the base flow (not shown). But the growth rates ($x \in [3.3, 3.8]$) and also the non-linear behaviour of mode $\beta = 36$ for $x > 3.9$ match perfectly.

For the *pinpoint suction* cases one hole with $v_{max} = -0.5 U_\infty$ is modeled at $x = 3.36$ with a diameter of $d = 0.0262$ which equals approximately the boundary-layer thickness and covers about 22% of one fundamental spanwise wavelength $\lambda_{z,0}$. The influence of the suction hole on the vortex strength ($\beta = 0 - (0,0)$) shows a touch more attenuation for the incompressible case (comparing red lines for case PP_i and red symbols for case PP_c). This observation is confirmed when looking at the high-frequency growth rate ($\beta = 90$) where the compressible one is slightly higher ($x \in [3.8, 4.1]$) whereas for the low-frequency mode identical growth rate attenuation is found. The overall agreement is excellent and the incompressible result is confirmed.

Regarding aspects like resolution, further downstream development of the attenuated secondary growth, or different suction scenarios with e.g. additional holes we note that the purpose of the current paper is verification and recommend reference [5] for further physical aspects. We note also that although $\Delta y_{wall,i} \approx 1/35 \Delta y_{wall,c}$ we find $\Delta t_i \approx 6 \Delta t_c$ and the numerical effort turns out to be still 10 times larger for the compressible method. Thus a case with rather small integration-domain extensions and resolution was chosen as verification case.

Fig. 5 shows a comparison of all four cases in physical space. Four snapshots of vortex-visualisations are shown in a rotated reference system. Additionally, the velocity components are shown in cross-cuts at three successive downstream locations. Albeit the weakening of the vortices is small for the cases with suction the

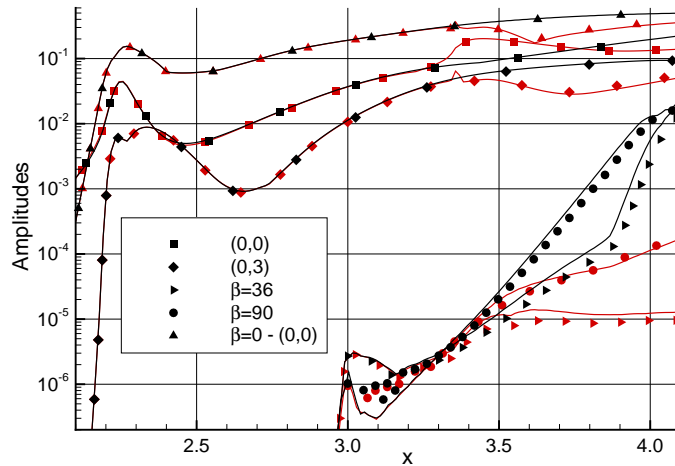


Fig. 4 Downstream development of selected modal \tilde{u}'_y -amplitudes from Fourier analysis in time (maximum over y and z). Shown are cases REF_i (black lines), REF_c (black symbols), PP_i (red lines), and PP_c (red symbols).

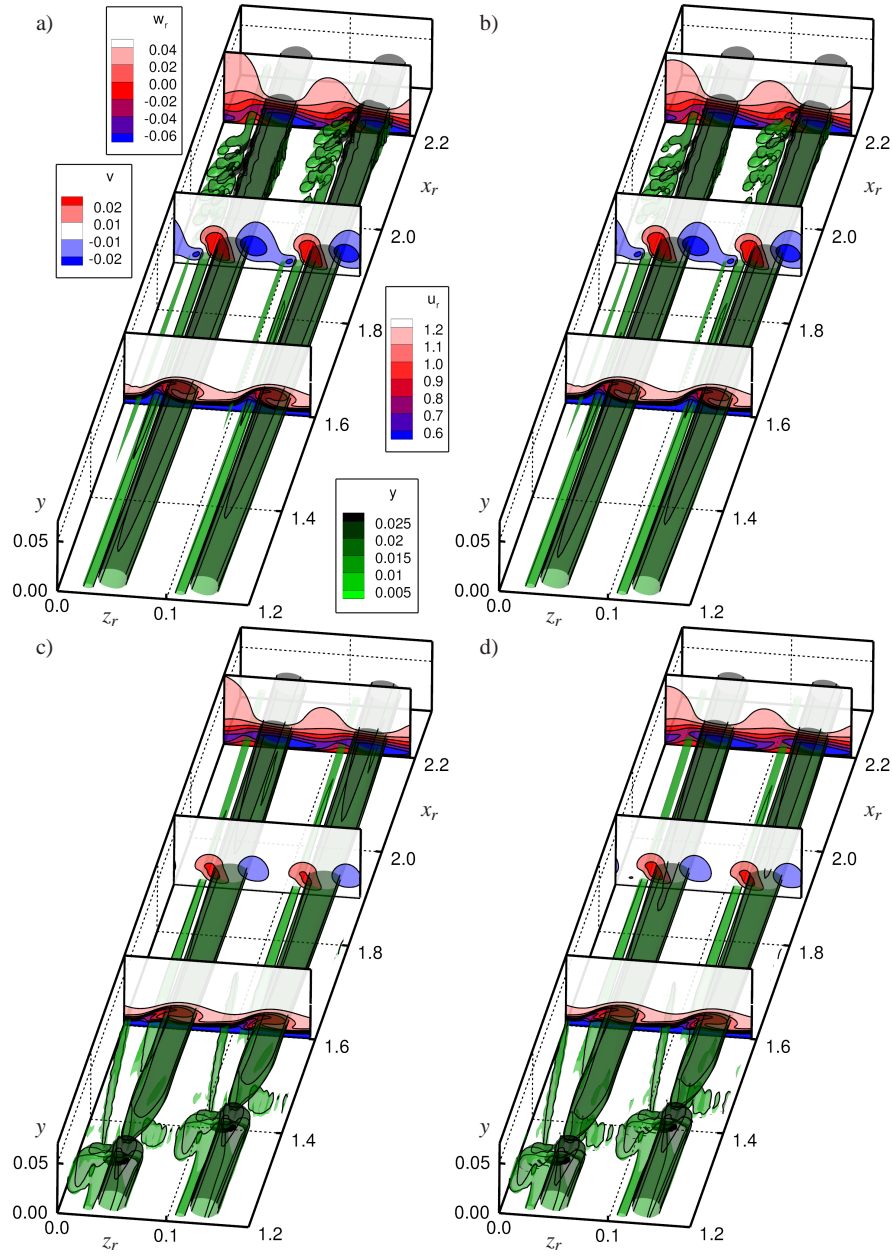


Fig. 5 Snapshots of crossflow-vortex visualisations ($\lambda_2=-5$) in a rotated reference system ($x_0 = 2.45$, $z_0 = 0.06$, $\phi_r = 45.0^\circ$, $x = x_0 + x_r \cdot \cos\phi - z_r \cdot \sin\phi$, $z = z_0 + z_r \cdot \cos\phi + x_r \cdot \sin\phi$) for cases a) *REF_i* b) *REF_c* c) *PP_i* d) *PP_c*. Shown are approximately two spanwise fundamental wavelengths. The suction holes in c) and d) are marked in black at $(x_r, z_r) = (1.3, 0.03)$ and $(1.4, 0.12)$.

effect in secondary instability is significant. Deviations between the reference cases are negligible. For the suction cases we observe minor differences in the vortex size downstream of the suction hole when comparing the y -levels for subpictures c) and d) which is already indicated in the amplitude plot. Again the agreement is excellent.

5 Conclusions

DNS results based on the incompressible vorticity-velocity formulation for crossflow-transition control by pinpoint suction have been successfully verified by compressible DNS. Despite the vorticity-velocity DNS needs a 35 times finer wall-normal resolution near the wall for a grid-independent result due to the high ($0.5 U_e$) suction velocity it is still by about one order of magnitude faster than the compressible DNS ($Ma=0.21$) for the investigated Prinzipexperiment problem ($Ma=0.04$). Most importantly however, the results for the attenuation of the high-frequency secondary instability match it being understood that it is sensitive to the crossflow-vortex induced shear layers. The next step is including suction channels.

The authors would like to thank O. Schmidt (IAG, University of Stuttgart) for providing the PNS code.

References

1. Babucke, A., Linn, J., Kloker, M.J., Rist, U.: Direct numerical simulation of shear flow phenomena on parallel vector computers. In High Performance Computing on Vector Systems 2005 (ed. M. Resch & al), Proc. High Performance Computing Center Stuttgart (HLRS), pp. 229-247, Springer (2006).
2. Bippes, H.: Basic experiments on transition in three-dimensional boundary layers dominated by crossflow instability, *Progress in Aerospace Sciences*, vol. 35, pp. 363–412, 1999.
3. Bonfigli, G., Kloker, M.J.: Secondary instability of crossflow vortices: validation of the stability theory by direct numerical simulation, *J. Fluid Mech.*, vol. 583, pp. 229–272, 2007.
4. Friederich, T., Kloker, M.J.: Localized blowing and suction for direct control of the crossflow secondary instability, Seattle AIAA-2008-4394.
5. Friederich, T., Kloker, M.J.: Direct Numerical Simulation of Swept-Wing Laminar Flow Control using Pinpoint Suction. In High Performance Computing in Science and Engineering '10: Transactions of the High Performance Computing Center, Stuttgart (HLRS) 2010 (eds. W.E. Nagel, D.B. Krner, M.M. Resch), in press, Springer (2011). Can be found at <http://www.iag.uni-stuttgart.de/IAG/people/tillmann.friederich>
6. Kloker, M.J.: Advanced Laminar Flow Control on a Swept Wing Useful Crossflow Vortices and Suction, Seattle AIAA-2008-3835.
7. Koch, W., Bertolotti, F. P., Stolte, A. and Hein, S.: Nonlinear equilibrium solutions in a three-dimensional boundary layer and their secondary instability, *J. Fluid Mech.*, vol. 406, pp. 131–174, 2000.
8. Linn, J., Kloker, M.J.: Numerical Investigations of Film Cooling. RESPACE - Key Technologies for Resuable Space Systems (ed. A. Gllhan), NNFM 98, pp. 151-169, Springer (2008).
9. Messing, R., Kloker, M.J.: Investigation of suction for laminar flow control of three-dimensional boundary layers, *J. Fluid Mech.*, vol. 658, pp. 117–147, 2010.
10. Peltzer, I., Wicke, K., Pätzold, A., Nitsche, W.: In-flight experiments on active TS-wave control on a 2D-laminar wing glove. *Seventh IUTAM Symposium on Laminar-Turbulent Transition*, Stockholm, Sweden, 2009 (ed. P. Schlatter & D. Henningson), Springer.
11. Carpenter, A.L., Saric, W.S., and Reed, H.L.: Laminar Flow Control on A Swept Wing With Distributed Roughness, AIAA 2008-7335.
12. Schrauf, G.: Status and perspective of laminar flow, The aeronautical journal (RAeAS), 109, no. 1102, 639-644.
13. Wassermann, P., Kloker, M.: Direct numerical simulation of the development and control of boundary-layer crossflow vortices. In *New Results in Numerical and Experimental Fluid Dynamics II* (ed. W. G. Nitsche, H.-J. Heinemann & R. Hilbig). *Proc. 11. AG STAB/DGLR Symposium (1998)*. Notes on Numerical Fluid Mechanics, vol. 72. Vieweg.
14. Wassermann, P., Kloker, M.J.: Mechanisms and passive control of crossflow-vortex-induced transition in a three-dimensional boundary layer, *J. Fluid Mech.*, vol. 456, pp. 49–84, 2002.
15. Wassermann, P., Kloker, M.J.: Transition mechanisms induced by travelling crossflow vortices in a three-dimensional boundary layer, *J. Fluid Mech.*, vol. 483, pp. 67–89, 2003.
16. White, E. B., Saric, W. S.: Secondary instability of crossflow vortices, *J. Fluid Mech.*, vol. 525, pp. 275–308, 2005.